ACS APPLIED MATERIALS & INTERFACES

Research Article

www.acsami.org

γ-Fe_2O_3 Nanocrystalline Microspheres with Hybrid Behavior of Battery-Supercapacitor for Superior Lithium Storage

Lei-Lei Tian,[†,‡] Ming-Jian Zhang,[†] Chao Wu,[‡] Yi Wei,[†] Jia-Xin Zheng,[†] Ling-Piao Lin,[†] Jun Lu,[§] Khalil Amine,[§] Quan-Chao Zhuang,[*,‡] and Feng Pan[*,†]

[†]Peking University, Shenzhen Graduate School, School of Advanced Materials, Shenzhen 518055, China

[‡]School of Materials Science and Engineering, China University of Mining & Technology, Xuzhou 221116, China

[§]Electrochemical Technology Program, Chemical Sciences and Engineering Division, Argonne National Laboratory, Argonne, Illinois 60439, United States

Supporting Information

ABSTRACT: Maghemite (γ-Fe_2O_3) nanocrystalline microspheres (MNMs) self-assembled with 52 nm nanocrystals bridged with FeOOH around grain boundaries were formed by solvothermal reaction and thermal oxidation. The unique architecture endows the MNMs with the lithium storage behavior of a hybrid battery-supercapacitor electrode: initial charge capacity of 1060 mAh g^{-1} at the 100 mA g^{-1} rate, stable cyclic capacity of 1077.9 mAh g^{-1} at the same rate after 140 cycles, and rate capability of 538.8 mAh g^{-1} at 2400 mA g^{-1}. This outstanding performance was attributed to the nanocrystal superiority, which shortens the Li^+ diffusion paths. The mechanism of this hybrid anode material was investigated with experimental measurements and structural analysis. The results indicate that at the first discharge, the MNM nanocrystal microsphere, whose structure can buffer the volume change that occurs during lithiation/delithiation, goes through four stages: Li^+ insertion in cation vacancies, spinel-to-rocksalt transformation, Li^+ intercalation of $Li_{1.75+x}Fe_2O_3$ nanocrystals, and interfacial Li storage around nanocrystal boundaries. Only the latter two stages were reversible at and after the second charging/discharging cycle, exhibiting the hybrid behavior of a battery-supercapacitor with superior lithium storage.

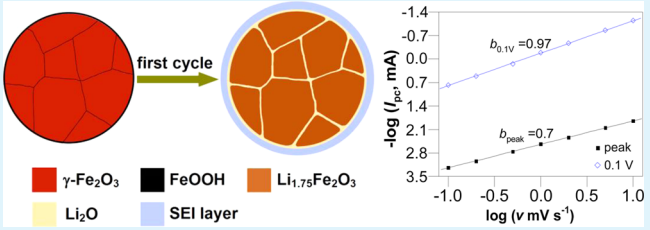

KEYWORDS: *ferric oxide, rate performance, interfacial capacitance, lithium ion battery, supercapacitor*

1. INTRODUCTION

To design advanced energy storage devices, we need electrode materials with very high energy and high power density. One possible path to that end is material engineering to combine the features of supercapacitors, which offer high rate performance, with rechargeable batteries, which offer high energy density.[1−4] Ferric oxides, by virtue of their much higher theoretical capacities and safety voltage window for avoiding formation of lithium dendrites, have long been intensively investigated as possible alternative electrode materials for lithium-ion batteries and supercapacitors.[5−12] However, even after decades of research, their commercialization is still hampered because their inherent electronic and ionic insulation, as well as large volume changes during the lithiation/delithiation processes,[13,14] result in rapid capacity degradation and poor rate capability. It is believed that enhancing the conductivity and the structural stability is the best strategy to circumvent these obstacles.[5−8] To date, nanosized ferric oxides and their carbonaceous hybrids have been intensively explored.[7−9,14−16] Although the reduction in particle size could shorten the electron transfer and Li^+ transport pathway to a certain extent,[5] the large exposed external surface for either nanosized crystals or carbonaceous hybrids would lead to unwanted interfacial reactions.[17] Moreover, the lithium storage performance of the obtained materials leaves much to be desired.

Maghemite (γ-Fe_2O_3) has an interesting crystal structure, in which the iron ions in the unit cell occupy the octahedral 16d and tetrahedral 8a sites of the space group $Fd\bar{3}m$ with different chemical states (Figure 1a). Although various researchers have studied the lithium storage mechanism and reversible conversion reaction of α-Fe_2O_3 anode material,[18−21] relatively little is known about the specific electrochemical reduction/oxidation processes for γ-Fe_2O_3 anode material, such as the lithium intercalation and the replacement of iron in the oxide framework. Herein, we discuss a hybrid battery-supercapacitor consisting of maghemite nanocrystalline microspheres (MNMs). The battery component provides reversible Li^+ intercalation/deintercalation in $Li_{1.75+x}Fe_2O_3$ nanocrystals during the lithiation/delithiation cycles, while the supercapacitor component provides intersecting grain boundaries with amorphous FeOOH throughout the microspheres that contribute an extra interfacial lithium storage capacity due to

Received: September 16, 2015
Accepted: November 9, 2015
Published: November 9, 2015

DOI: 10.1021/acsami.5b08756
ACS Appl. Mater. Interfaces 2015, 7, 26284−26290

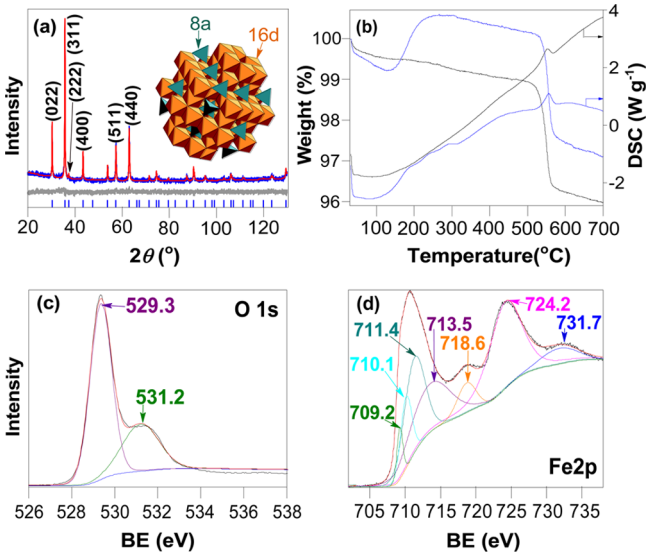

Figure 1. (a, black) Observed and (red) Rietveld calculated XRD results and (inset) unit cell structure of MNM; (b) TG-DSC results of (blue line) FOM and (black line) MNM; high-resolution XPS of (c) O 1s and (d) Fe 2p spectra for MNM.

the large internal grain boundaries. Furthermore, the microsphere structures can buffer the volume change that occurs during lithiation/delithiation and thereby maintains a stable structure, and the nanocrystals with large boundaries could significantly reduce the Li^+ diffusion pathway and expedite the ion transport. All these properties combine to achieve superior electrochemical performance in terms of reversible capacity, cycle life, and rate capability.

2. EXPERIMENTAL SECTION

2.1. Sample Synthesis. All the chemicals are of analytical grade and were used without further purification. The maghemite (γ-Fe_2O_3) nanocrystalline microspheres (MNMs) were obtained by thermal oxidization of hierarchical structured ferroferric oxide (Fe_3O_4) microspheres (FOMs), while the latter was synthesized by a solvothermal reaction. In a typical synthesis, 9.56 g $NaAc{\cdot}3H_2O$ and 2.16 g $FeCl_3{\cdot}6H_2O$ were gradually added into 64 mL of ethylene glycol under vigorous stirring successively, and then 1.42 mL of polyethylene glycol (PEG) 200 was added. The adequately dispersed suspension was transferred into a Teflon-lined stainless steel autoclave and sealed. After holding at 190 °C for 8 h followed by furnace cooling naturally, the products were separated by centrifugation, repeatedly washed with deionized water and anhydrous ethyl alcohol, and air-dried at 45 °C. The formation mechanisms of hierarchical-structured FOMs are generally illustrated as nucleation-oriented aggregation-recrystallization processes.[21−24] The obtained FOMs were further heated in air atmosphere at 400 °C for 4 h to transform into MNMs.

2.2. Material Characterization. The crystallographic structures of the samples were determined by a Bruker AXS D8 X-ray diffractometer with Cu Kα radiation at λ = 0.15405 nm. The X-ray diffraction (XRD) pattern for Rietveld analysis was recorded from 20 to 130° by a step-scanning method with 0.02° step width and 2 s sampling time. The XRD pattern of MNMs was analyzed by Rietveld method using the TOPAS3 software of Bruker AXS. $Fd\bar{3}m$ was employed as the space group to represent the structure model.[22] Electrodes with different lithiation states for XRD were prepared by charge/discharge to the designated potentials and equilibrated at that potential for 1 h to attain steady-state conditions, rinsed with dimethyl carbonate, and then sealed with paraffine.

Transmission electron microscopy (TEM) images were captured on a JEOL-2010 instrument at an acceleration voltage of 200 kV, and scanning electron microscopy (SEM) characterizations were performed on a field emission JSM-6700F instrument. The cycled electrodes for the SEM and TEM survey were pre-equilibrated at 3.0 V for 1 h to attain steady-state conditions. X-ray photoelectron spectroscopy (XPS) (ESCALAB 250 Xi; Al anode X-ray source) was used to investigate the surface chemistries of the obtained materials, while the surface areas and porosities were measured by the standard nitrogen adsorption isotherms at 77 K using an automated Micropore gas analyzer ASAP 2020 (Micromeritics Instruments). Thermogravimetry (TG) and differential scanning calorimetry (DSC) analyses were carried out with a simultaneous thermal analyzer (TG/DSC 1, Mettler Toledo), in which the dried material was heated in oxygen atmosphere at 10 °C min^{-1} from room temperature to 700 °C.

2.3. Electrochemical Characterization. The working electrodes were prepared by spreading a mixture of active mass (60 wt %), acetylene black (20 wt %), and polyvinylidene fluoride (20 wt %, Kynar FLEX 910, Elf Atochem) binder dissolved in *N*-methylpyrrolidone (Fluka Inc., St. Louis, MO) onto a Cu foil (thickness, 20 μm) current collector. The electrolyte consists of 1 M $LiPF_6$ in a mixture of isometric ethylene carbonate, dimethyl carbonate, and diethyl carbonate (Guotai-Huarong Co., Zhangjiagang, China). The electrochemical characterizations were conducted in 2025-type coin cells using Li foil (99.9%, China Energy Lithium Co., Ltd., Tianjin) as the counter electrode. Galvanostatic charge−discharge (GCD) experiments were conducted on a battery testing system (CT2001A, Land) over a range of 0.05−3 V versus Li/Li^+. The reported specific capacity (SC) data were all normalized to the weight of active materials. Cyclic voltammetry (CV) measurements were performed on an electrochemical workstation (CHI 660D) within the range of 0.05−3 V. Before the CV tests, the electrode was preactivated for 10 GCD cycles.

3. RESULTS AND DISCUSSION

As shown in Figure 1a and Figure S1, the framework of γ-Fe_2O_3 is similar to that of Fe_3O_4. It has eight molecules per unit cell. All of the O^{2-} anions are located at the (32e) sites of the space group $Fd\bar{3}m$ as a cubic close-packed array. The Fe^{3+} cations occupy all of the tetrahedral (8a) and partial of the octahedral (16d) sites, and the other octahedral (16d) sites are vacant. This material is represented by the formula $Fe_{(8a)}[Fe_{5/3}\square_{1/3}]_{(16d)}O_4$. The XRD results of MNM were Rietveld analyzed using the structure model of Fe_3O_4 (ICSD-1513304) in the $Fd\bar{3}m$ space group to estimate the Fe^{3+} occupancy in 16d sites. The real occupancy of Fe^{3+} in 16d sites was calculated to be 0.8358 nm (Table S1), that is, very close to the theoretical value (0.833 nm), and thus the occupancy of vacancies in 16d sites was 0.1642. The calculated unit cell dimension (a = 0.8346 nm) of MNM is smaller than that of Fe_3O_4 (a = 0.840 nm). This difference is due to the smaller layer spacing and O−O distances caused by the cation vacancies in the γ-Fe_2O_3 framework,[23,24] which transform Fe_3O_4 to γ-Fe_2O_3 with thermal oxidation. The Fourier-transform infrared (FT-IR) spectra could provide more effective proofs to the differentiated symmetry grounds of Fe_3O_4 and γ-Fe_2O_3. As presented in Figure S2a, the FT-IR spectrum of the FOM displays an intense band at around 595 cm^{-1} with a broad shoulder up to 800 cm^{-1}, the main band is attributed to the Fe−O band, and the shoulder to the amorphous FeOOH. By contrast, the FT-IR spectrum of the MNM shows more complicated features at around 630 and 550 cm^{-1}, indicating the disordered vacancy in O_h sites. The vacancy ordering is reported to change the symmetry of the spinel phase or to appear without distortion of the cubic cell, and thus revealing the additional bands.[25,26]

The results from TG and DSC provided additional information about the structural features of the samples (Figure 1b). The TG curve indicated that the greatest mass enhancement of FOM occurs between 200 and 315 °C,

DOI: 10.1021/acsami.5b08756
ACS Appl. Mater. Interfaces 2015, 7, 26284−26290

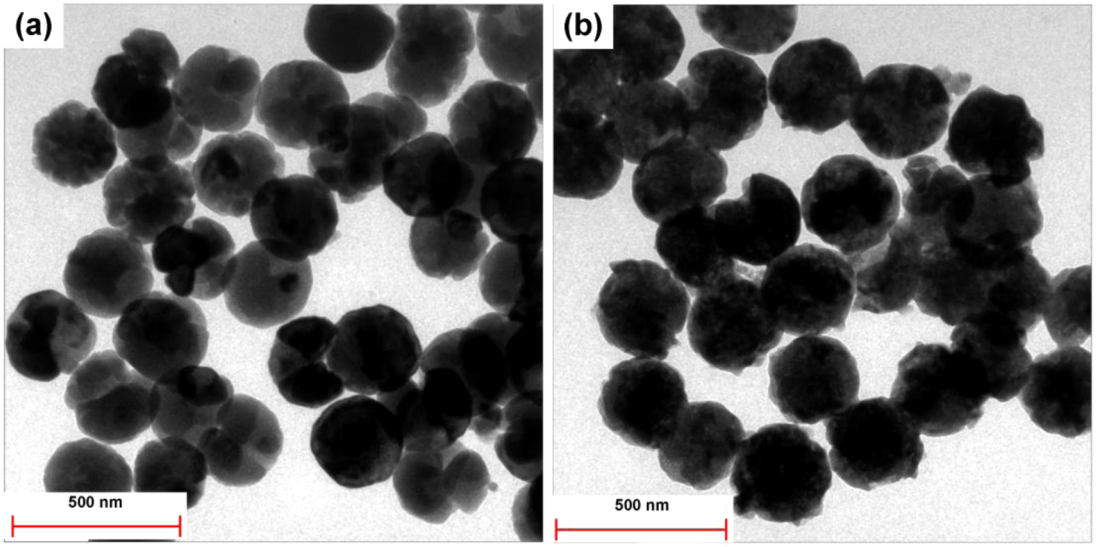

Figure 2. Representative TEM images of (a) FOM and (b) MNM.

corresponding to the broad exothermic stage on the DSC curve. We ascribed this effect to the oxidization of Fe_3O_4 to γ-Fe_2O_3. Interestingly, Figure 1b shows exothermic peaks at around 553 °C with the small mass loss (ca. 3%) for both MNM and FOM. These peaks could be attributed to the dehydroxylation process accompanied by phase transformation from γ-Fe_2O_3 to α-Fe_2O_3, as confirmed by the XRD and TG results (Figure S3). It was reported that hydroxyl groups could coordinate to the underlying Fe atoms in the crystal surface, due to its structural integrity, and thus form FeOOH.[27] The FeOOH composition is produced around the microsphere surface and the primary grain boundaries of FOM during the solvothermal synthesis, and is accompanied by the phase transformation from FOM to MNM.[28,29] We also confirmed these FeOOH structures by XPS. The binding energy (BE) data obtained by XPS (Figures 1c,d) were corrected with the C 1s reference line at 284.8 eV. The O 1s region of the oxyhydroxide would show a doublet with one peak due to oxide and the other hydroxide. The O 1s spectrum of the MNM gives peak maxima at 529.3 eV along with weak peak at 531.2 eV, suggesting the different coordinations of oxygen. The main peak is coming from the oxide lattice of γ-Fe_2O_3, while the weak peak is corresponding to the hydroxyl of FeOOH and surface absorbed H_2O of γ-Fe_2O_3.[7,28] The Fe $2p_{3/2}$ (lower BE) and Fe $2p_{1/2}$ (higher BE) main peaks are clearly accompanied by satellites on their higher BE sides. The peaks at 711.4 and 713.5 eV that arise from the Fe $2p_{1/3}$ spectrum were assigned to the Fe^{3+} bond with O^{2-} in the crystal lattice and with −OH in the grain surface, respectively, while the other peaks at lower bonding (709.2 and 710.1 eV) were assigned to trace Fe^{2+} in MNM.[30−32] In addition, the FT-IR spectrum of MNM (Figure S2) could provide other evidence of FeOOH, the asymmetry broad band at round 3440 and another broad shoulder at around 800 cm^{-1} could be assigned to the hydrogen bonded −OH groups of amorphous FeOOH.[25] While the free bulk FeOOH could not exist under calcination at 400 °C, the enclosed FeOOH in the grain-boundaries of γ-Fe_2O_3 nanocrystals might be maintained due to the restricted condition. Furthermore, the surface Fe atoms may be coordinatively unsaturated under calcination condition, which could be coordinated with hydroxyl ions or water molecules and thus formed FeOOH on the surface of γ-Fe_2O_3 nanocrystals when the samples cooling down.

The nitrogen adsorption−desorption results (Figures S4a,b) show no significant difference between MNM and FOM, and the pore-size distribution (Figure S4c) indicates no apparent pore-size distribution peak for either MNM or FOM. The BET specific surface areas of the MNM and FOM (derived from Figure S4d) are 9.4 and 9.9 $m^2\ g^{-1}$, respectively. These results indicate that the primary grains bridged with amorphous FeOOH and are closely packed in the microspheres.

The FOM obtained directly from the solvothermal reaction appeared as uniform microspheres with a diameter of ca. 230 nm, as shown by the transmission electron micrographs in Figure 2 and scanning electron micrographs in Figure S5. It has been speculated that PEG molecules used in material fabrication make the nanocrystals self-assemble into sphere-like aggregating entities due to the hydroxyl groups of PEG as the structure-directing agent.[33] After being heated at 400 °C for 4 h in air, the FOM is transformed into MNM, the latter maintains the morphology of FOM. In spite of the volume change from Fe_3O_4 to γ-Fe_2O_3 of 110% (derived from a theoretical calculation), it is difficult to discern this change from the electron-microscopic images. The average size of the primary nanocrystal γ-Fe_2O_3 particles was calculated as ca. 52 nm from the XRD results.

The MNM was GCD cycled at a current density of 100 mA g^{-1} over the voltage range of 0.05−3.0 V versus Li/Li^+. As shown in Figure 3a, the SCs for the first discharge and charge are 1765.4 and 1060 mAh g^{-1}, respectively. The first discharge curve could be partitioned into four regions with voltage ranges of 3−1.2, 1.2−0.9, 0.9−0.6, and 0.6−0.05 V, corresponding to SCs of 48.3 (I), 256.4 (II), 784.3 (III), and 676.4 (IV) mAh g^{-1}, respectively. The structure evolutions of the MNM electrode during each region were surveyed by ex situ XRD. As shown in Figure 4, all diffraction peaks shift ca. 0.3° toward lower angle (2θ) when the MNM electrode was discharged to 1.2 V, indicating a structural expansion of the unit cell. This effect was attributed to Li^+ insertion in 16d octahedral vacancies and formation of $Fe_{(8a)}[Fe_{5/3}Li_{1/3}]_{(16d)}O_4$, as follows:

DOI: 10.1021/acsami.5b08756
ACS Appl. Mater. Interfaces 2015, 7, 26284−26290

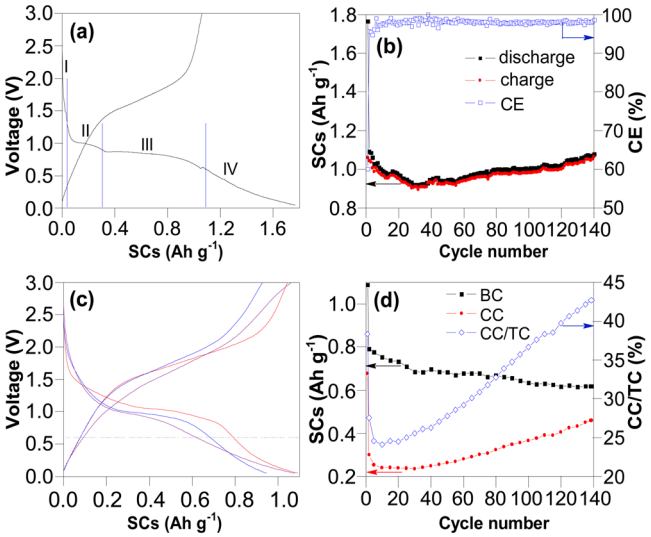

Figure 3. Electrochemical characterization of a half-cell composed of MNM electrode over the voltage range 0.05−3.0 V at a current density of 100 mA g^{-1}. (a) Charge−discharge voltage profiles for the first cycle; (b) SC and Coulombic efficiency (CE) over 140 cycles; (c) voltage profiles for the (red) 2nd, (blue) 30th, and (purple) 140th cycles; (d) battery capacity (BC) and capacitive capacity (CC) and efficiency over 140 cycles.

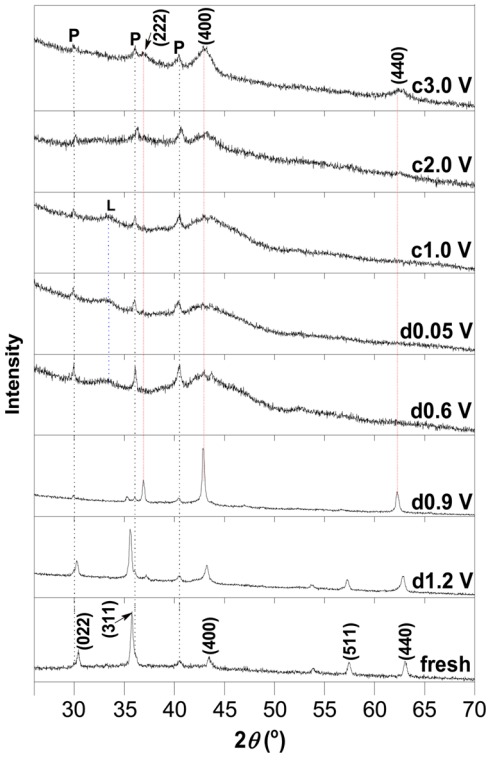

Figure 4. Ex situ XRD patterns of MNM electrodes with different lithiation states. L = Li_2O; P = paraffine; d = discharge; c = charge.

$$Fe_{(8a)}[Fe_{5/3}\square_{1/3}]_{(16d)}O_4 + 1/3Li^+ + 1/3e^- \rightarrow Fe_{(8a)}[Fe_{5/3}Li_{1/3}]_{(16d)}O_4 \quad (1)$$

After the electrode was discharged to 0.9 V, the relative intensity of the (311), (220), and (422) diffraction peaks was reduced; conversely, the relative intensity of the (400), (440), and (222) peaks was considerably increased. The (400), (440), and (222) planes of the γ-Fe_2O_3 unit cell in $Fd\bar{3}m$ space group are constituted of closely packed 16d and 16c sites (Figure 5). We concluded that tetrahedral 8a sites Fe^{3+} are displaced by octahedral 16c sites accompanying the Li^+ insertion, and this process forms $Li_{(8a)}[FeLi]_{(16c)}[Fe_{5/3}Li_{1/3}]_{(16d)}O_4$ (represented as $Li_{1.75}Fe_2O_3$) according to the reaction in eq 2, which is known as the spinel-to-rocksalt transformation.[34,35] The theoretical specific capacity according to the eq 2 is 293.6 mAh g^{-1}, the experimental discharge capacity of the corresponding voltage range is 256.4 mAh g^{-1}, the little difference of the two values might be because of the incomplete reaction of electrode materials.

$$Fe_{(8a)}[Fe_{5/3}Li_{1/3}]_{(16d)}O_4 + 2Li^+ + 2e^- \rightarrow Li_{(8a)}[FeLi]_{(16c)}[Fe_{5/3}Li_{1/3}]_{(16d)}O_4 \quad (2)$$

After discharge to 0.6 V, a new broad XRD peak, assigned to Li_2O (JCPDF No. 12-0254), emerged at around 33° (Figure 4), corresponding to the electrochemical reduction of FeOOH at nanocrystal boundaries. The XRD pattern at 0.05 V is identical with that at 0.6 V. This indicates no further insertion or conversion reaction after region III; thus, region IV could be ascribed to interfacial lithium storage. Note that the (400) XRD peaks during cycles can be detected consistently, and the (400), (440), and (222) peaks can be reboosted after the first charge (see 3.0 V charge pattern in Figure 4 and Figure S6b). We concluded that the framework related to the (400) plane in $Li_{1.75+x}Fe_2O_3$ ($0 < x < 4.25$) nanocrystals could be maintained after further Li^+ insertion in the vacancies at 8b and 48f sites, and the $Li_{1.75}Fe_2O_3$ can be regenerated during the charge reaction. Consequently, the reversible reaction during the subsequent cycles can be represented by the reaction in eq 3, corresponding to a theoretical SC of 713 mAh g^{-1}.

$$Li_{(8a)}[FeLi]_{(16c)}[Fe_{5/3}Li_{1/3}]_{(16d)}O_4 + xLi^+ + xe^- \rightleftarrows Li_{(8a)}Li_{(8b)}[Li_{x-1}]_{(48f)}[FeLi]_{(16c)}[Fe_{5/3}Li_{1/3}]_{(16d)}O_4 \quad (0 < x < 5.67) \quad (3)$$

The Li^+ insertion in vacancies and the spinel-to-rocksalt transformation during the first discharge are irreversible, with a theoretical SC loss of 29.2%. Thus, the lower first-cycle CE (60%) of the MNM electrode (Figure 3b) could be mainly attributed to these irreversible reactions.[5,36,37] In addition, the electrolyte decomposition and formation of solid state interface layers on the surface of the microspheres, as verified by the SEM and TEM results (Figure 6), could also contribute to the capacity loss.[5]

CV at different scan rates was performed to survey the lithium storage behavior of the MNM. As shown in Figure 7, a cathodic peak appeared at about 0.9 V at a scan rate of 1 mV s^{-1}. This peak gradually shifted to lower potential by increasing the scan rate, corresponding to the Li^+ intercalation as discussed above. Large capacitive current could be distinguished at the potential range below 0.6 V. The detailed CV information in the different voltage regimes was analyzed by measuring the variation of current (I) with scan rate (v) according to the power law $I = a * v^b$, where a and b are adjustable coefficients.[38] A b value of 0.5 means that the electrode reaction is controlled by semi-infinite linear diffusion and a value of 1 indicates that the reaction is limited by surface processes. As shown in Figure 7b, when the scan rate was increased from 0.1 to 10 mV s^{-1}, the b value at cathode peak

DOI: 10.1021/acsami.5b08756
ACS Appl. Mater. Interfaces 2015, 7, 26284−26290

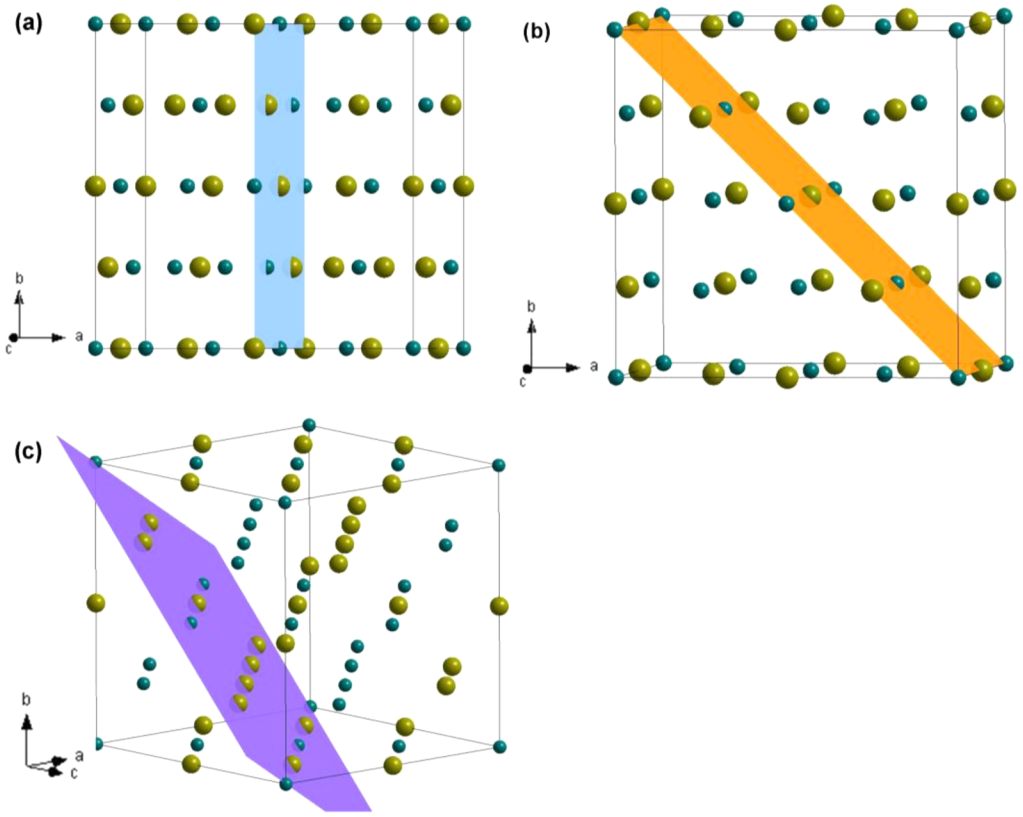

Figure 5. (a) (400), (b) (440), and (c) (222) planes of γ-Fe_2O_3 unit cell in $Fd\bar{3}m$ space group. Larger spheres denote 16d sites; smaller spheres denote 16c sites.

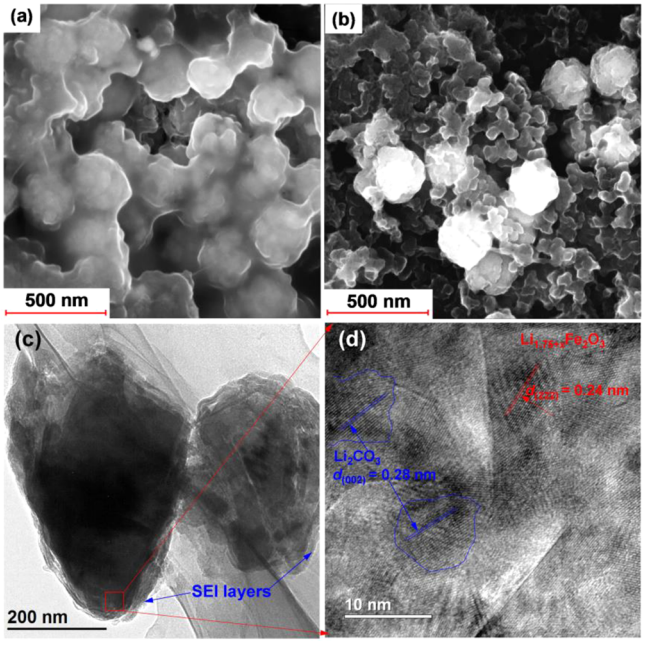

Figure 6. SEM images of MNM electrode after (a) 30 GCD cycles and (b) electron impact decomposed the solid-electrolyte interphase (SEI) layer; (c) TEM and (d) high-resolution TEM images of MNM electrode after 300 GCD cycles.

was determined to be 0.7, corresponding to a hybrid of diffusion-limited current and surface-process-limited current, whereas the *b* value at 0.1 V was determined to be 0.97, indicating a pure capacitive current at lower potential.

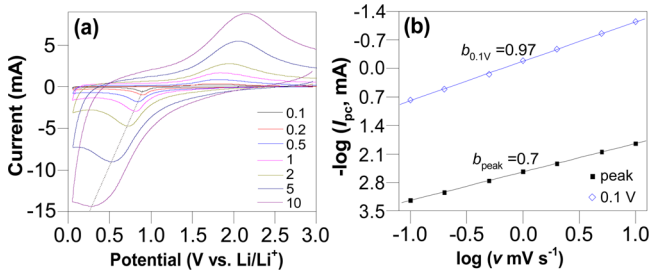

Figure 7. (a) CV curves at different scan rates for MNM electrode from 0.1 to 10 mV s^{-1} over the potential range of 0.05−3 V vs Li/Li^+, and (b) *b*-value determination of the absolute peak and 0.1 V cathodic current.

During the long-term cycles, the discharge capacity of the MNM electrode gradually decreased until 30th cycle and then increased from 919.3 (30th cycle) to 1077.9 (140th cycle) mAh g^{-1}. Based on the analysis for CV results, the discharge capacity above 0.6 V (vs Li/Li^+) can be assigned to the BC resulting from Li^+ intercalation in $Li_{1.75+x}Fe_2O_3$, and the capacity below 0.6 V (vs Li/Li^+) can be associated with the CC resulting from the Li^+ adsorption on the interfaces between $Li_{1.75+x}Fe_2O_3$ and Li_2O around the nanocrystal boundaries.[39,40] As indicated in Figure 3d, there is a reciprocal relationship between the BC and the CC during electrochemical cycling. The BC gradually declined from 678.4 (30th cycle) to 617.7 (140th cycle) mAh g^{-1}, yet the CC increased from 234.9 (30th cycle) to 460.2 (140th cycle) mAh g^{-1} and delivered 42.7% of the total capacity (TC) at 140th cycle, these were in accordance with the CV results as presented in Figure S7.

DOI: 10.1021/acsami.5b08756
ACS Appl. Mater. Interfaces 2015, 7, 26284−26290

The MNM rate capabilities were also investigated as shown in Figure 8. The initial charge capacity was 942.6 mAh g^{-1} at a

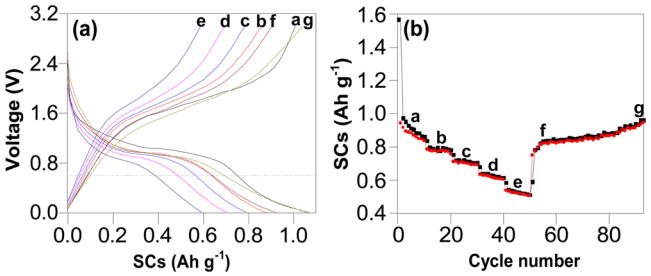

Figure 8. Rate capabilities of MNM electrode over the voltage range of 0.05−3.0 V. (a) Charge−discharge voltage profiles and (b) rate performance. Curves in these figures are at (a) 0.15, (b) 0.3, (c) 0.6, (d) 1.2, and (e) 2.4 A g^{-1}; also (f) 60th and (g) 94th cycle at 0.15 A g^{-1}.

current density of 150 mA g^{-1}, and then decreased to 787.3, 712.3, 634.3, and 538.8 mAh g^{-1} at current densities of 300, 600, 1200, and 2400 mA g^{-1}, respectively. A higher charge capacity of 947.7 mAh g^{-1} was obtained when the current density was reduced back to 150 mA g^{-1} after 93 cycles. Furthermore, the MNM electrode showed impressive long-term rate performance: stable capacities of 242.5 mAh g^{-1} (235th cycle) and 113.3 mAh g^{-1} (530th cycle) were delivered at rates 3 and 6 A g^{-1}, respectively, and there was no obvious capacity fading even at the 736th cycle (Figure S6). These superior rate capabilities are rarely reported for bare Fe_2O_3 materials (Table S2). We attributed it to the highly stable structures of both the $Li_{1.75+x}Fe_2O_3$ nanocrystals and the microspheres assembled with the nanocrystals for the anode electrode, as shown in Figure 5 and 6. The detailed microstructure evolution of MNM was proposed as follows (Figure S8): fresh MNM is constructed with several γ-Fe_2O_3 primary grains (nanocrystals with 52 nm size), which are densely bridged with amorphous FeOOH around the grain boundaries; the unique structure of the polycrystal-packed microspheres could efficiently buffer the structural strain of the primary grains and accommodate the volume variation of the microspheres associated with cyclic lithiation/delithiation, thus giving a high cyclic stability; after several lithiation/delithiation cycles, a polymeric SEI layer would coat the microsphere; this coating would prevent further decomposition due to electrolyte on primary grain surfaces and thus maintain an open surface structure among different grains in a single MNM; furthermore, the lithiation reaction would start from the grain boundaries due to the lower energy barrier, and the resulting amorphous Li_2O intersecting the $Li_{1.75}Fe_2O_3$ in the microsphere could form a fast Li^+ transport network and expedite ion transport;[41,42] during long-term electrochemical cycling, the microsphere would remain intact due to the support of the compact polymeric layer.

4. CONCLUSIONS

We prepared MNM self-assembled with 52 nm nanocrystals bridged with amorphous FeOOH around grain boundaries by thermal oxidation of the precursor, FOM, which was synthesized by solvothermal reaction. The resulting MNM achieved outstanding stable performance: initial reversible capacity of 1060 mA h g^{-1} at a current density rate of 100 mA g^{-1}, stable cyclic capacity of 1077.9 mAh g^{-1} at the same rate after around 140 cycles, and a rate capability of 538.8 mA h g^{-1} at 2400 mA g^{-1}. The mechanism of the high-performance anode material is attributed to (1) the nanocrystals and interface structure of the microsphere, which shorten the Li^+ diffusion paths; (2) the microspheres buffering the volume change during lithiation/delithiation; and (3) the reversible Li^+ intercalation/deintercalation in $Li_{1.75+x}Fe_2O_3$ nanocrystals and interfacial Li storage around nanocrystal boundaries. This electrode material thus exhibits hybrid behavior of a battery-supercapacitor for superior lithium storage. Hence, this work illustrates a new strategy in designing and forming novel electrode materials for a high-performance Li-ion battery.

■ ASSOCIATED CONTENT

Supporting Information

The Supporting Information is available free of charge on the ACS Publications website at DOI: 10.1021/acsami.5b08756.

Structural parameters of MNM obtained from Rietveld refinement and additional figures. (PDF)

■ AUTHOR INFORMATION

Corresponding Authors

*E-mail: panfeng@pkusz.edu.cn.

*E-mail: zhuangquanchao@126.com.

Notes

The authors declare no competing financial interest.

■ ACKNOWLEDGMENTS

The authors acknowledge financial support from the Fund from the National Project for EV Batteries (20121110, Optimum Nano, Shenzhen), the Guangdong Innovation Team Project (No. 2013N080), and the Shenzhen Science and Technology Research Grant (No. ZDSY20130331145131323, CXZZ20120829172325895, JCYJ20150629144526408). The authors are also grateful to the Test Engineer Hai-Wen Zhang for assistance with TG-DSC and nitrogen adsorption measurements.

■ REFERENCES

(1) Tian, L. L.; Wei, X. Y.; Zhuang, Q. C.; Jiang, C. H.; Wu, C.; Ma, G. Y.; Zhao, X.; Zong, Z. M.; Sun, S. G. Bottom-Up Synthesis of Nitrogen-Doped Graphene Sheets for Ultrafast Lithium Storage. *Nanoscale* **2014**, *6*, 6075−6083.

(2) Simon, P.; Gogotsi, Y.; Dunn, B. Where do Batteries End and Supercapacitors Begin? *Science* **2014**, *343*, 1210−1211.

(3) Vlad, A.; Singh, N.; Rolland, J.; Melinte, S.; Ajayan, P. M.; Gohy, J. F. Hybrid Supercapacitor-Battery Materials for Fast Electrochemical Charge Storage. *Sci. Rep.* **2014**, *4*, 4315.

(4) Zhao, X.; Hayner, C. M.; Kung, M. C.; Kung, H. H. In-Plane Vacancy-Enabled High-Power Si-Graphene Composite Electrode for Lithium-Ion Batteries. *Adv. Energy Mater.* **2011**, *1*, 1079−1084.

(5) Larcher, D.; Bonnin, D.; Cortes, R.; Rivals, I.; Personnaz, L.; Tarascon, J. M. Combined XRD, EXAFS, and Mössbauer Studies of the Reduction by Lithium of α-Fe_2O_3 with Various Particle Sizes. *J. Electrochem. Soc.* **2003**, *150*, A1643−A1650.

(6) Zhou, W.; Lin, L.; Wang, W.; Zhang, L.; Wu, Q.; Li, J.; Guo, L. Hierarchial Mesoporous Hematite with "Electron-Transport Channels" and Its Improved Performances in Photocatalysis and Lithium Ion Batteries. *J. Phys. Chem. C* **2011**, *115*, 7126−7133.

(7) Tian, L.; Zhuang, Q.; Li, J.; Wu, C.; Shi, Y.; Sun, S. The Production of Self-Assembled Fe_2O_3-Graphene Hybrid Materials by a Hydrothermal Process for Improved Li-Cycling. *Electrochim. Acta* **2012**, *65*, 153−158.

DOI: 10.1021/acsami.5b08756
ACS Appl. Mater. Interfaces 2015, 7, 26284−26290

(8) Wu, C.; Zhuang, Q. C.; Tian, L. L.; Wu, Y. X.; Ju, Z. C.; Zhang, H.; Zhang, X. X.; Chen, H. B. Synthesis and the Comparative Lithium Storage Properties of Hematite: Hollow Structures vs. Carbon Composites. *RSC Adv.* **2015**, *5*, 21405−21414.
(9) Wu, C.; Zhang, H.; Wu, Y. X.; Zhuang, Q. C.; Tian, L. L.; Zhang, X. X. Synthesis and Characterization of Fe@Fe_2O_3 Core-Shell Nanoparticles/Graphene Anode Material for Lithium-Ion Batteries. *Electrochim. Acta* **2014**, *134*, 18−27.
(10) Ke, F. S.; Huang, L.; Zhang, B.; Wei, G. Z.; Xue, L. J.; Li, J. T.; Sun, S. G. Nanoarchitectured Fe_3O_4 Array Electrode and Its Excellent Lithium Storage Performance. *Electrochim. Acta* **2012**, *78*, 585−591.
(11) Yang, P.; Ding, Y.; Lin, Z.; Chen, Z.; Li, Y.; Qiang, P.; Ebrahimi, M.; Mai, W.; Wong, C. P.; Wang, Z. L. Low-Cost High-Performance Solid-State Asymmetric Supercapacitors Based on MnO_2 Nanowires and Fe_2O_3 Nanotubes. *Nano Lett.* **2014**, *14*, 731−736.
(12) Ma, Z.; Huang, X.; Dou, S.; Wu, J.; Wang, S. One-Pot Synthesis of Fe_2O_3 Nanoparticles on Nitrogen-Doped Graphene as Advanced Supercapacitor Electrode Materials. *J. Phys. Chem. C* **2014**, *118*, 17231−17239.
(13) Lin, Y. M.; Abel, P. R.; Heller, A.; Mullins, C. B. α-Fe_2O_3 Nanorods as Anode Material for Lithium Ion Batteries. *J. Phys. Chem. Lett.* **2011**, *2*, 2885−2891.
(14) Hang, B. T.; Watanabe, I.; Doi, T.; Okada, S.; Yamaki, J. I. Electrochemical Properties of Nano-Sized Fe_2O_3-Loaded Carbon as a Lithium Battery Anode. *J. Power Sources* **2006**, *161*, 1281−1287.
(15) Hu, J.; Zheng, J.; Tian, L.; Duan, Y.; Lin, L.; Cui, S.; Peng, H.; Liu, T.; Guo, H.; Wang, X.; Pan, F. A Core-Shell Nanohollow-γ-Fe_2O_3@Graphene Hybrid Prepared Through the Kirkendall Process as a High Performance Anode Material for Lithium Ion Batteries. *Chem. Commun.* **2015**, *51*, 7855−7858.
(16) Wu, C.; Zhuang, Q.; Tian, L.; Cui, Y.; Zhang, X. Facile Synthesis of Fe@Fe_2O_3 Core-Shell Nanoparticles Attached to Carbon Nanotubes and Their Application as High Performance Anode in Lithium-Ion Batteries. *Mater. Lett.* **2013**, *107*, 27−30.
(17) Aricò, A. S.; Bruce, P.; Scrosati, B.; Tarascon, J. M.; Van Schalkwijk, W. Nanostructured Materials for Advanced Energy Conversion and Storage Devices. *Nat. Mater.* **2005**, *4*, 366−377.
(18) Larcher, D.; Masquelier, C.; Bonnin, D.; Chabre, Y.; Masson, V.; Leriche, J. B.; Tarascon, J. M. Effect of Particle Size on Lithium Intercalation into α-Fe_2O_3. *J. Electrochem. Soc.* **2003**, *150*, A133−A139.
(19) Jain, G.; Balasubramanian, M.; Xu, J. J. Structural Studies of Lithium Intercalation in a Nanocrystalline α-Fe_2O_3 Compound. *Chem. Mater.* **2006**, *18*, 423−434.
(20) Reddy, M. V.; Yu, T.; Sow, C. H.; Shen, Z. X.; Lim, C. T.; Subba Rao, G. V.; Chowdari, B. V. R. α-Fe_2O_3 Nanoflakes as an Anode Material for Li-ion Batteries. *Adv. Funct. Mater.* **2007**, *17*, 2792−2799.
(21) Wang, B.; Chen, J. S.; Wu, H. B.; Wang, Z. Y.; Lou, X. W. Quasiemulsion-Templated Formation of alpha-Fe_2O_3 Hollow Spheres with Enhanced Lithium Storage Properties. *J. Am. Chem. Soc.* **2011**, *133*, 17146−17148.
(22) Yamauchi, S.; Hibino, M.; Yao, T. Structure Change Analysis in γ-Fe_2O_3/Carbon Composite in the Process of Electrochemical Lithium Insertion. *Solid State Ionics* **2011**, *191*, 45−48.
(23) Cornell, R. M.; Schwertmann, U., Crystal Structure. In *The Iron Oxides*; Wiley-VCH Verlag GmbH & Co. KGaA: Weinheim, 2004; pp 9−38.
(24) Zhang, X.; Niu, Y.; Meng, X.; Li, Y.; Zhao, J. Structural Evolution and Characteristics of the Phase Transformations Between α-Fe_2O_3, Fe_3O_4 and γ-Fe_2O_3 Nanoparticles Under Reducing and Oxidizing Atmospheres. *CrystEngComm* **2013**, *15*, 8166−8172.
(25) Krehula, S.; Music, S. Influence of Ruthenium Ions on the Precipitation of alpha-FeOOH, alpha-Fe_2O_3 and Fe_3O_4 in Highly Alkaline Media. *J. Alloys Compd.* **2006**, *416*, 284−290.
(26) Daou, T. J.; Greneche, J. M.; Pourroy, G.; Buathong, S.; Derory, A.; Ulhaq-Bouillet, C.; Donnio, B.; Guillon, D.; Begin-Colin, S. Coupling Agent Effect on Magnetic Properties of Functionalized Magnetite-Based Nanoparticles. *Chem. Mater.* **2008**, *20*, 5869−5875.
(27) Cornell, R. M.; Schwertmann, U., Surface Chemistry and Colloidal Stability. In *The Iron Oxides*; Wiley-VCH Verlag GmbH & Co. KGaA: Weinheim, 2004; pp 221−252.
(28) Maiti, D.; Manju, U.; Velaga, S.; Devi, P. S. Phase Evolution and Growth of Iron Oxide Nanoparticles: Effect of Hydrazine Addition During Sonication. *Cryst. Growth Des.* **2013**, *13*, 3637−3644.
(29) Sanders, J. P.; Gallagher, P. K. Kinetics of the Oxidation of Magnetite Using Simultaneous TG/DSC. *J. Therm. Anal. Calorim.* **2003**, *72*, 777−789.
(30) Wu, P.; Du, N.; Zhang, H.; Yu, J.; Yang, D. Carbon Nanocapsules as Nanoreactors for Controllable Synthesis of Encapsulated Iron and Iron Oxides: Magnetic Properties and Reversible Lithium Storage. *J. Phys. Chem. C* **2011**, *115*, 3612−3620.
(31) Grosvenor, A. P.; Kobe, B. A.; Biesinger, M. C.; McIntyre, N. S. Investigation of Multiplet Splitting of Fe 2p XPS Spectra and Bonding in Iron Compounds. *Surf. Interface Anal.* **2004**, *36*, 1564−1574.
(32) Yamashita, T.; Hayes, P. Analysis of XPS Spectra of Fe^{2+} and Fe^{3+} Ions in Oxide Materials. *Appl. Surf. Sci.* **2008**, *254*, 2441−2449.
(33) Qiu, Y.; Xu, G. L.; Yan, K.; Sun, H.; Xiao, J.; Yang, S.; Sun, S. G.; Jin, L.; Deng, H. Morphology-Conserved Transformation: Synthesis of Hierarchical Mesoporous Nanostructures of Mn_2O_3 and the Nanostructural Effects on Li-Ion Insertion/Deinsertion Properties. *J. Mater. Chem.* **2011**, *21*, 6346−6353.
(34) Pernet, M.; Strobel, P.; Bonnet, B.; Bordet, P.; Chabre, Y. Structural and Electrochemical Study of Lithium Insertion Into γ-Fe_2O_3. *Solid State Ionics* **1993**, *66*, 259−265.
(35) Bonnet, B.; Strobel, P.; Pernet, M.; Gondrand, M.; Gros, Y.; Mouget, C.; Chabre, Y. Structural Aspects of Lithium Insertion into γ-Fe_2O_3. *Mater. Sci. Forum* **1992**, *91*−*93*, 345−350.
(36) Morales, J.; Sánchez, L.; Martín, F.; Berry, F.; Ren, X. Synthesis and Characterization of Nanometric Iron and Iron-Titanium Oxides by Mechanical Milling: Electrochemical Properties as Anodic Materials in Lithium Cells. *J. Electrochem. Soc.* **2005**, *152*, A1748−A1754.
(37) Wu, X. L.; Guo, Y. G.; Wan, L. J.; Hu, C. W. α-Fe_2O_3 Nanostructures: Inorganic Salt-Controlled Synthesis and Their Electrochemical Performance Toward Lithium Storage. *J. Phys. Chem. C* **2008**, *112*, 16824−16829.
(38) Balaya, P.; Li, H.; Kienle, L.; Maier, J. Fully Reversible Homogeneous and Heterogeneous Li Storage in RuO_2 with High Capacity. *Adv. Funct. Mater.* **2003**, *13*, 621−625.
(39) Jamnik, J.; Maier, J. Nanocrystallinity Effects in Lithium Battery Materials: Aspects of Nano-Ionics. Part IV. *Phys. Chem. Chem. Phys.* **2003**, *5*, 5215−5220.
(40) Zhang, J.; Huang, T.; Liu, Z.; Yu, A. Mesoporous Fe_2O_3 Nanoparticles as High Performance Anode Materials for Lithium-Ion Batteries. *Electrochem. Commun.* **2013**, *29*, 17−20.
(41) Balke, N.; Jesse, S.; Morozovska, A. N.; Eliseev, E.; Chung, D. W.; Kim, Y.; Adamczyk, L.; García, R. E.; Dudney, N.; Kalinin, S. V. Nanoscale Mapping of Ion Diffusion in a Lithium-Ion Battery Cathode. *Nat. Nanotechnol.* **2010**, *5*, 749−754.
(42) Zhu, X.; Ong, C. S.; Xu, X.; Hu, B.; Shang, J.; Yang, H.; Katlakunta, S.; Liu, Y.; Chen, X.; Pan, L.; Ding, J.; Li, R. W. Direct Observation of Lithium-Ion Transport Under an Electrical Field in Li_xCoO_2 Nanograins. *Sci. Rep.* **2013**, *3*, 1084.

DOI: 10.1021/acsami.5b08756
ACS Appl. Mater. Interfaces 2015, 7, 26284−26290